



Volume estimation and evaluation of rotational landslides using multi-temporal aerial photographs in Çağlayan dam reservoir area, Turkey

Tümay Kadakci Koca¹ · M. Yalcin Koca¹

Received: 1 August 2018 / Accepted: 25 January 2019 / Published online: 16 February 2019
© Saudi Society for Geosciences 2019

Abstract

Four landslide scarps in Neogene sedimentary rocks were observed in the Çağlayan dam reservoir area. This study aims to (1) estimate the volume of landslide material that slid into the dam reservoir area within 59-year period and (2) evaluate the reactivations with respect to triggering and predisposing factors such as slope gradient, precipitation, fire, and seismic activity. In this context, field survey was combined with innovative use of multi-temporal historical aerial photographs. Various methods of photogrammetry were employed on four sets of stereo aerial photographs (1953, 1970, 1995, 2012) to identify the boundaries of landslides, to generate digital elevation models (DEMs) from which cross-sectional data and slope maps were extracted. Volumes of landslides were estimated based on height differences between successive DEMs. Spatial mismatch and height errors between successive DEMs were minimized by image to image coregistration and height adjustment, respectively. The height adjustment technique was reevaluated and it was suggested to choose 11 sub-areas independent from the size and location. It is also recommended that the accuracy of the landslide boundaries interpreted from aerial photographs should be cross-checked by overlapped cross-sections of successive years to estimate the volume more precisely. A total volume of $121.78 \times 10^4 \text{ m}^3$ material collapsed whereas the largest volume moved in the period between 1953 and 1970 which was linked to a seismic event. Unconsolidated debris and weak rock layers are expected to fail in relation to water level fluctuations in the dam lake. The volume of sliding material will contribute to siltation and shorten the operational life of Çağlayan dam.

Keywords Aerial photograph · Multi-temporal analyses · Photogrammetry · Rotational slide · Volume estimation

Introduction

The landslides in dam reservoir area have caused severe damages in the history. Therefore, detailed geological and geotechnical investigation of reservoir slopes and generating digital elevation model (DEM) of landslide affected area (Yu et al. 2016) is crucial for hazard mitigation. Volume estimation of old landslides in the dam reservoir area is also essential to anticipate the potential of a possible hazard.

Landslide volume determination is a difficult task that requires information on the surface and sub-surface geometries

of the slope failure (Guzzetti et al. 2009). A considerable amount of literature has been published on estimating the volume of a landslide. For example, Cruden and Varnes (1996) and Marchesini et al. (2009) have used the ellipsoid approach to determine volumes of rotational landslides. This method assumes a regular shaped landslide body that is being a portion of an ellipsoid. Nikolaeva et al. (2014) revised the ellipsoid approach and adapted the method to rock slides that possess translational components. All of the above approaches require information on the depth of rupture surface or the depth of displaced material which can only be provided from in situ methods such as borehole and inclinometric measurements or geophysical investigations. Gathering this information is expensive and time consuming and may be very challenging due to steep slopes (Malamud et al. 2004). Conversely, the information on the area of the landslides can be rapidly and simply provided from aerial photographs or satellite images. Several studies thus far have linked volume to area of landslides (Malamud et al. 2004; Guzzetti et al.

Editorial handling: Zeynal Abiddin Erguler

✉ Tümay Kadakci Koca
tumay.koca@deu.edu.tr

¹ Geological Engineering Department, Engineering Faculty, Dokuz Eylul University, 35390 Izmir, Turkey

2009; Larsen et al. 2010; Fuller et al. 2016; Amirahdi et al. 2016). They found that there is a strong relationship between the area (A) and the volume (V) of displaced material independent from local physiographical setting (Eq. 1). The term displaced material has been defined by IAEG Commission on Landslides (1990) as the material displaced from its original position on the slope by movement in the landslide and it is referred to the sum of depleted mass and the accumulation (Fig. 1).

$$V = \alpha \times A^\gamma \quad (1)$$

where α and γ are empirical constants. Larsen et al. (2010) stated that small differences in γ lead to substantial variance in volume estimations. In addition, there is no general agreement about selecting proper scaling exponent (γ) for landslides involving both debris and rock. In the case of reactivations that occur in different portions of the initial landslide body, the areal extension of the reactivated portion may not be recognized on the aerial photograph. Thus, the empirical equations and the ellipsoid approach would be inadequate.

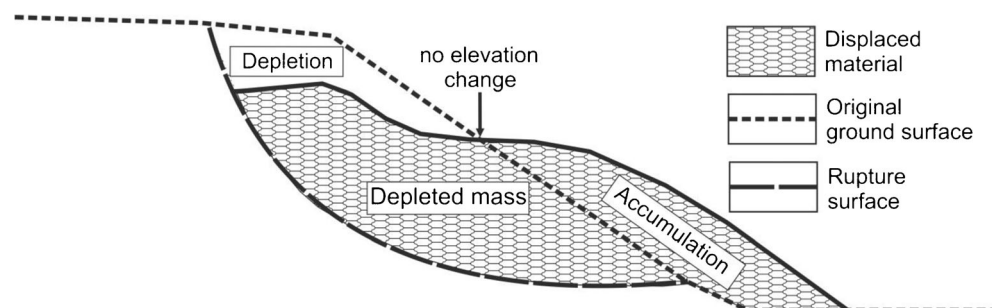
Unlike the conventional methods based on geometrical assumptions and empirical equations, subtracting the DEMs of two successive years is a useful tool to obtain volumes of landslides (Huang et al. 2015). The older DEM is subtracted from the recent one and the resultant differential DEM can be evaluated in terms of the negative and positive height differences. The positive values refer to increment in height and thus the accumulated (fill) volume whereas the negative values refer to decrease in height and thus the collapsed (cut) volume. De Bari et al. (2011) combined the ellipsoid approach with results from differential DEMs. They have argued that the ellipsoid volume refers to the volume of depleted mass since there is a part in landslide body named “filling up” volume that no elevation change is detected (Fig. 1). Therefore, De Bari et al. (2011) suggested that the total volume of displaced material after the movement can only be obtained by adding the volume of depletion and accumulation calculated from differential DEMs to the ellipsoid volume. Nevertheless, the results obtained from this approach do not match with the definition of volume of displaced material suggested by IAEG Commission on Landslides (1990). On the other hand, the authors concluded

that the volume of moved material (mass transfer) is equal to either volume of depletion or the volume of accumulation.

Several researchers have used height difference model (HDM) which is based on simply the multiplication of elevation differences with corresponding pixel sizes for estimating volume from differential DEMs (Coe et al. 1997; Van Westen and Getahun 2003; Tsutsui et al. 2007; Du and Teng 2007; Corsini et al. 2009). It should be noted that HDM enables calculation of only collapsed and accumulated material volumes and does not take into account the depleted mass. One major limitation of HDM is that the errors in the plane positions and height value and height baseline difference between two DEMs may reduce the accuracy of the results produced by this model (Chen et al. 2014). A broader perspective has been adopted by Chen et al. (2006) who improved the HDM to minimize the height errors between two DEMs. The new method was referred to as the advanced height difference model (AHDM) by Chen et al. (2014). This model assumes that if there is no height error between two DEMs, the elevation difference should be zero outside the landslide prone area. In this context, sub-areas are selected to control the elevation differences between two DEMs. The average height differences in the sub-areas are considered to be systematic height errors between successive DEMs. Subsequently, the differential DEMs are adjusted for the average height differences. According to Chen et al. (2014), standards do not exist for choosing appropriate sub-areas however; the average height adjustment value obtained from sub-areas has a significant effect on the volume calculations. Chen et al. (2014) further improved the AHDM to a mass balance model (MBM) which is based on mass balance principle. They argued that MBM provides more accuracy on volume estimation where there is no material loss and there is no filling up volume. However, mass balance is not provided for a wide range of landslides particularly for landslides along riverbanks.

The volume of displaced material is not necessary when dealing with the sediment input volume into the lake of the dam. It is obvious that only a portion of the whole landslide body slides into the reservoir whereas the depleted mass remains on the rupture surface (Fig. 1). In passive form since a portion of accumulated material is washed out by an agent (stream flow).

Fig. 1 The illustration of the parts of a landslide body (modified after De Bari et al. 2011)



On the other hand, evaluation of predisposing and triggering factors of an old landslide provides an insight to the conditions required for the slope to fail. For example, rainfall is a common trigger for landslides on both natural and engineered slopes (Cai and Ugai 2004; Martinović et al. 2018; Wang et al. 2018). Rainfall infiltration leads an increase in groundwater level and pore water pressure and thus reduces the effective stress and the shear strength of earth material that may result in rainfall-induced slope failures. Various researchers stated that the high-intensity rainfalls increase the possibility of relative landslides (Bai et al. 2013; Vardon 2015). On the other hand, extreme rainfalls during a short time may not totally infiltrate and cause runoff. Wildfires decrease the infiltration rates and therefore advance the hillslope sediment transport by runoff processes. Due to the loss of vegetation roots and organic cover, the decrease in soil shear strength, and the changes in hydrologic properties, non-cohesive surface material becomes vulnerable to erosion (Gabet 2003). While the shear strength of the sub-surface soil or rock masses reduced due to weathering, extensive rainfall, and wildfire, an earthquake can trigger the failure (Hack et al. 2007). Heavy seismic damage tends to occur in water-saturated slopes due to the fact that groundwater induces the slope failure at a lower horizontal seismic intensity (Lu et al. 2015).

In this study, field methodology was combined with innovative use of multi-temporal historical aerial photos in order to estimate the volume of four rotational landslides and evaluate the variation of collapsed and accumulated volumes in different time periods with respect to triggering and predisposing factors (e.g., slope gradient, precipitation, fire, and seismic activity). The effect of image to image coregistration and

height adjustment on the reliability of volumetric analyses also examined. The ambiguity in choosing elevation control sub-areas was investigated.

The study area

Geological setting

The focus of the study is a 1.22-km² area within the valley of Kayacık stream. The Çağlayan dam site is located in the western part of Turkey, between the Gediz Graben and the Akhisar-Akselendi and Gölarmara Fault zones (Fig. 2). The region is characterized by E-W (e.g., Gediz, Küçük Menderes, and Büyük Menderes grabens) trending Quaternary basins as a result of N-S extension of the western Anatolia and their basin-bounding active strike-slip and normal faults (Özkaymak et al. 2013; Hakyemez et al. 2013). These prominent structures commonly dominate the landscape in the region. The closest active fault to the dam site is Pleistocene Akpınar Fault that is located in 2.4 km west of the study area. It is a NW-SE trending strike-slip fault having a length of approximately 18 km (Fig. 2). In regional scale, active landslides are generally located on the hanging wall of the normal faults. Landslides close to the study area (minimum: 11.86 km) are classified as old landslides and rarely active landslides (Duman et al. 2011).

The oldest rock outcrop in the region is Keçiadağ Formation which is composed of schist and marble of Menderes Massif metamorphic rocks. The stratigraphic sequence continues with Neogene-aged Göcek Formation, Yeniköy Formation, Küçükderbent Formation, Ahmetler Formation, and Quaternary alluvium and slope debris, respectively (Fig. 3).



Fig. 2 Location map of the study area and the active faults around the study area (retrieved from Emre et al. 2013)

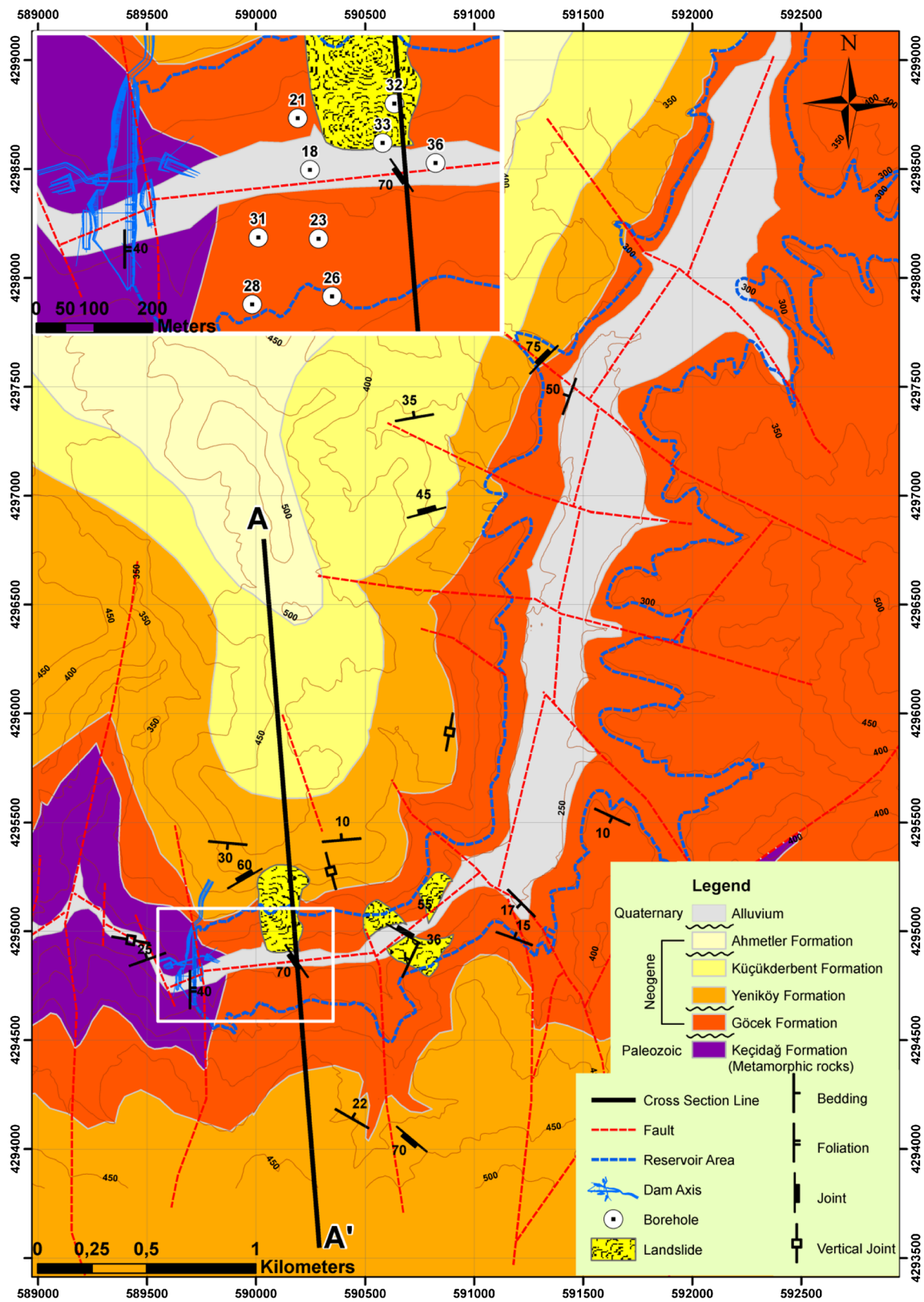


Fig. 3 Geological map of the study area

Göcek Formation mainly consists of non-compacted conglomerate, siltstone, mudstone, cross-bedded and weakly

cemented sandstone and limestone with algae. Göcek Formation is unconformably overlaid by Yeniköy Formation

which dominantly includes sandstone, conglomerate, and argillaceous limestone with claystone intercalations. The hillslopes are covered by Quaternary slope debris.

There are four landslides in the dam reservoir area (Fig. 4). Three of them are on the northern bank (landslide-1, 2, and 4) and the other one (landslide-3) is on the southern bank of the reservoir area.

Landslide-1 is dominantly composed of sandstone, mudstone, limestone, and conglomerate of Yeniköy and Göcek Formation. Landslide-2 and 4 are composed of sandstone, siltstone, and conglomerate intercalations of Göcek Formation. Landslide-3 dominantly consists of highly fractured limestone of Göcek Formation with unfilled, opened joints (max. 20 cm). Open-joint walls work as a pathway for water flow particularly during and after heavy rainfall. The toes of the landslides intersect the Kayacık streambed. The valley of Kayacık River is formed by E-W trending normal faults which are overlapping the axis of anticline and illustrated in a geological cross-section passing through the Landslide-1 constructed according to the borehole data and field observations (Fig. 5). Similarly to the tectonics of Aegean region in the western part of Turkey, NE-SW trending thrust faults and NW-SE trending normal faults are controlling the geostructural features in the dam site (Fig. 3).

Field investigations were carried out to measure the discontinuity properties and to examine the logs of boreholes. The logs of nine boreholes provided additional information

about geological units and their thicknesses. Two out of nine boreholes are located in the streambed (BH-18, 36); three boreholes are on the northern bank of the reservoir area (BH-21, 32, 33) and the others on the southern bank (BH-23, 26, 28, and 31) (Fig. 3). The depths of the boreholes are ranging between 15 and 50 m. The maximum thickness of the highly fractured and partially disintegrated (RQD = 0–50%) sedimentary rocks is 23 m with a mean of 9 m. The rock units are mantled by unconsolidated, coarse-grained slope debris with a thickness of 1.3 to 15 m in southern bank and 2 to 6 m in northern bank. In the streambed, the first 6 m below the ground level is composed of alluvium with a maximum grain size of 20–30 cm. The materials transported and deposited by the landslide range from gravel to several meter-sized blocks of limestone at the toe of Landslide-3 (Fig. 6).

BH-32 and 33 are located in the lower part (accumulation zone) of Landslide-1. Breccia zone was intersected between the depths 9 and 16 m below the ground surface in BH-33 and between 15 and 23 m in BH-32 (Fig. 7).

The altitudes range from 220 to 480 m for the highest point on the upper parts of the southern faced slopes (Landslide-1, 2, 4). The catchment area is approximately 1.22 km² (Fig. 8). The northern part of the catchment has a gentle slope; however, it is steeper in the area where the landslides occur. In the landslide prone area, the slope angles are ranging between 10° and 49.5°.

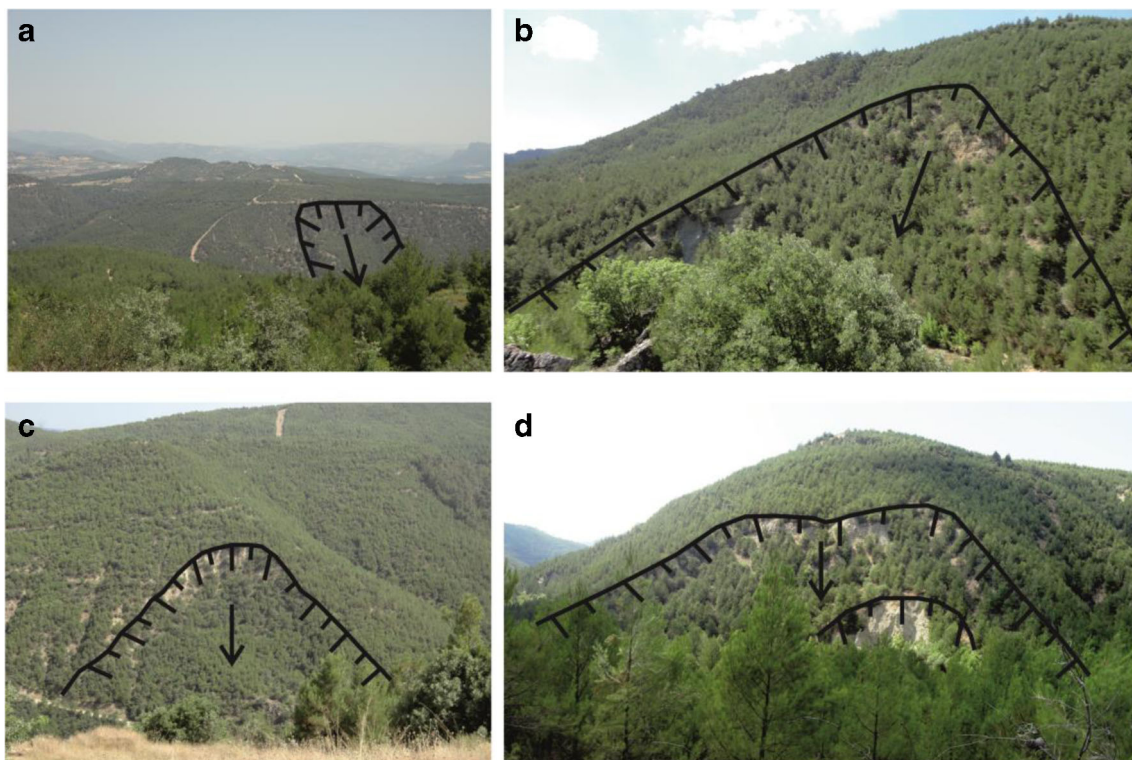


Fig. 4 Landslides observed in the Çağlayan dam site. **a** Landslide-1. **b** Landslide-2. **c** Landslide-3. **d** Landslide-4

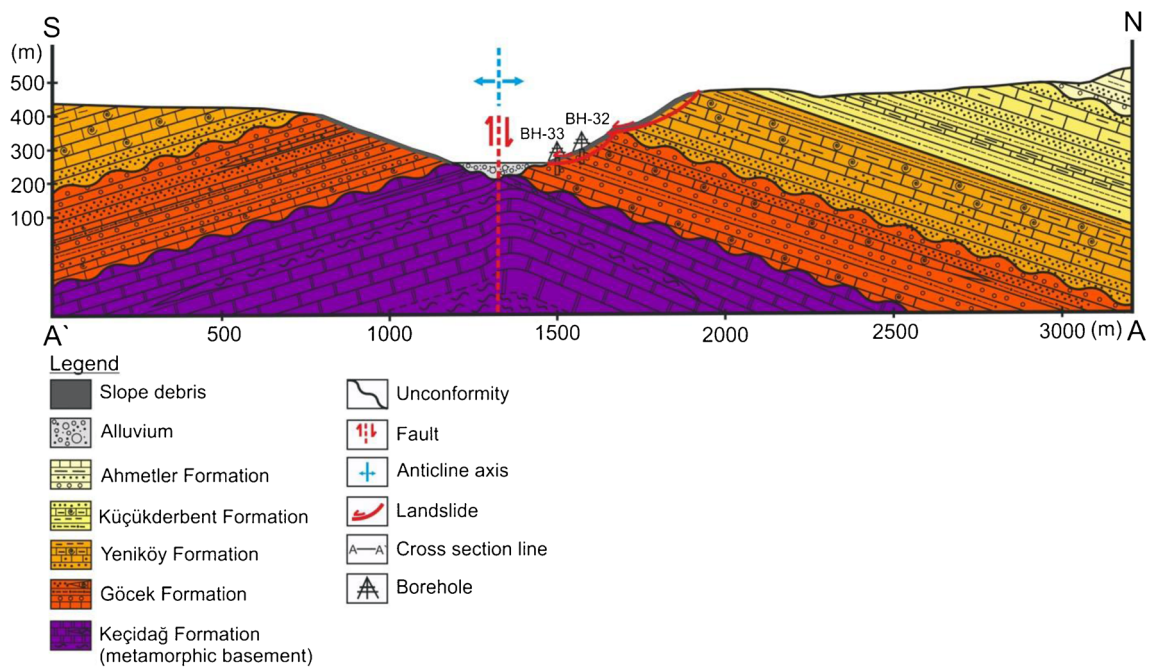


Fig. 5 Geological cross section of A-A' constructed through the Landslide-1

Climate

The climate of Manisa can be classified as humid, mesothermal, and large summer efficiency according to the classification proposed by Thornthwaite (1948). Mean monthly precipitation ranges from 4.7 to 147.2 mm. Precipitation records indicate that 89% of annual precipitation falls between October and April. The amount of precipitation significantly decreased between the years 1989 and 1994. However, it passed over the mean value (706.4 mm) in the following years with fluctuations in every 2 years (Fig. 9). In slope stability point of view, excessive daily rainfall is important for landslide triggering. The maximum daily rainfall in the period of 1929–2012 is 163.5 mm (23 December 1986). It is greater than



Fig. 6 Rock blocks removed by the mass movements

the mean monthly precipitation value of December. It should be noted that it was not possible to identify the amount of rainfall within the catchment area. In addition, in 1988 summer, a wildfire affected the northern and southern hillslopes of Kayacık River. Shrubs, deciduous, and coniferous trees within 1190 ha area were destroyed by the wildfire.

Seismicity

Manisa city is involved in the first-degree earthquake zone. The seismic event data from 1900 to 2017 in the radius of 100 km in the dam site is illustrated in Fig. 10.

As the earthquake magnitudes greater than four are considered, the earthquakes having moment magnitude (M_w) between 4 and 5 are 76.2% of the total recorded 373 earthquakes. The earthquakes having moment magnitudes greater than 6 are only 2.8%.

The greatest earthquake in the region is Alaşehir earthquake that occurred on 28 March 1969 with a moment magnitude of 6.5 at 4 km depth. The epicenter of the earthquake is located at approximately 40 km southeast of the dam site. According to earthquake attenuation relationships proposed by Ulusay et al. (2004), the peak ground acceleration for the site due to this earthquake was approximately 102 gal. Another shallow earthquake occurred along Akpınar Fault located approximately 2.4 km east of the study area at a depth of 10 km on 30 September 1965. It had a moment magnitude of 5.0 and caused a peak ground acceleration of 78 gal. The earthquakes that have $M_w > 4$, depth ≤ 10 km, and distance to the study area ($R \leq 40$ km) are listed in Table 1.

Fig. 7 The core box of BH-32 between the depth 15 and 21 m showing the breccia zone



Methods

Field investigations

The discontinuity properties were described by means of field observations according to ISRM (2007). The dominant joint sets and bedding planes were defined on the basis of measured dip angle and dip direction of discontinuities excluding the random joints. The discontinuity orientations were projected on the Schmidt net (equal area projection) via Dips software (Rocscience 2010). During core drilling, water pressure tests were carried out and the permeability of the sedimentary rocks is expressed in terms of Lugeon (LU) values. Ghafoori et al. (2011) stated that in order to describe or estimate the

permeability of jointed rock, the result of water pressure test should be converted to permeability coefficient (k) value instead of LU value. LU values obtained from the tests were converted to k by the conversion factor given below:

$$1 \text{ Lugeon} = 1.3 \times 10^{-5} \text{ cm/s} \tag{2}$$

Photogrammetry

Four sets of multi-temporal, stereo aerial photographs (1953, 1970, 1995, and 2012) were used in order to quantify the surface area of landslides over time and to generate digital elevation models (DEMs). The available acquisition

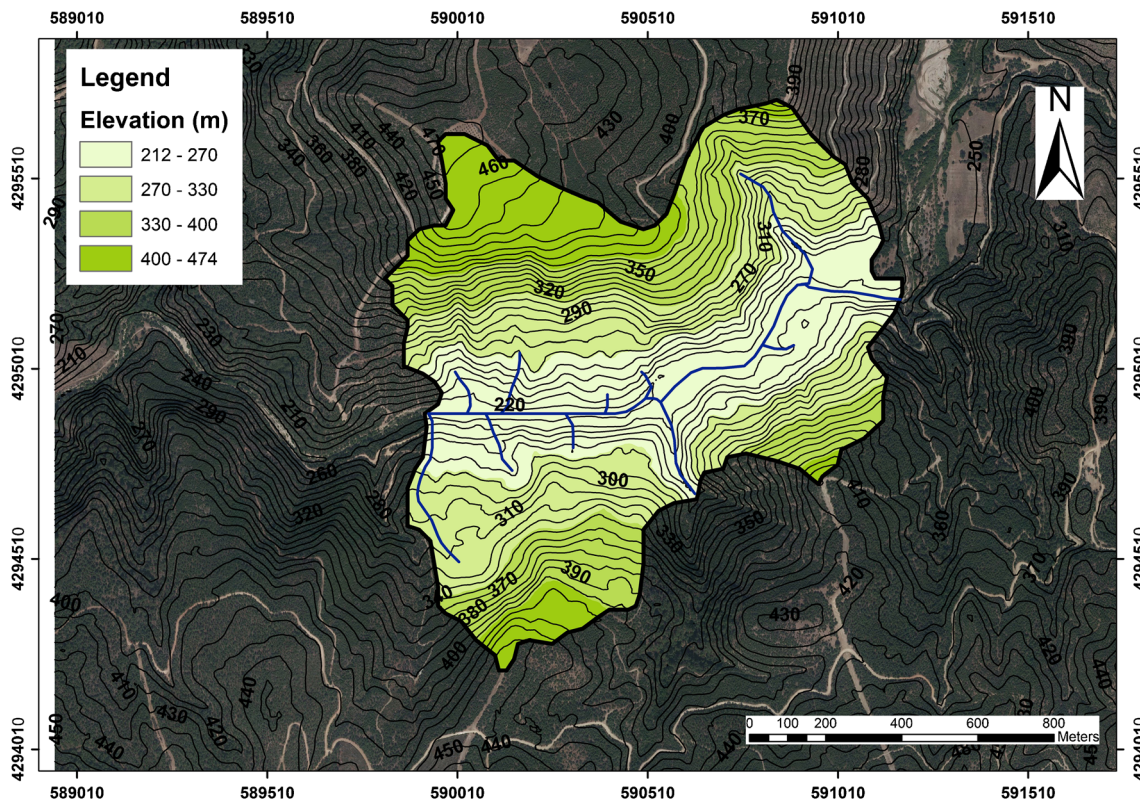
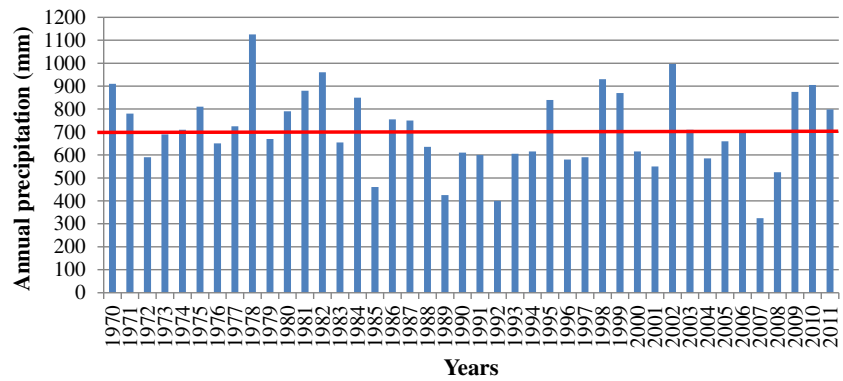


Fig. 8 Watershed boundaries of landslide prone area

Fig. 9 Mean annual precipitation records for the years between 1970 and 2011 (the red line refers to the mean annual precipitation of all years)



parameters for the historical aerial photographs and the digital photograph are given in Table 2.

Initially, the aerial photographs were georeferenced to a common base map (1/25,000 topographical map) individually. Each photograph was adapted to the Universal Transverse Mercator (UTM) map projection (Zone 35N), the World Geodetic System (WGS) 1984 horizontal datum, and the WGS 1984 ellipsoid. Following the georeferencing process, orthorectification was performed via orthoengine module of PCI Geomatica software (PCI Geomatics 2012). Orthorectification process requires acquisition parameters that are rarely available for archival photographs. The unknown acquisition parameters cause mis-registrations between the orthorectified images to be compared (Ayoub et al. 2009). In this context, the 2012 aerial photograph with spatial resolution of 0.3 m was selected as the base image. The acquisition parameters of warp images (1953, 1970, 1995) were improved by optimizing with respect to the base image (2012). Image to image coregistration was therefore performed by manually identifying

the common points (tie points) in both images such as individual trees, pathway intersections, and corners of farmlands. As a result of image to image coregistration, the pixel sizes of the warp images were the same as those of the base image.

Polygons of four landslide bodies were digitized through the interpretation of aerial photographs by using ArcGIS software (ESRI 2015). The main scarps of landslides were identified on aerial photographs by the aid of brighter and white colored pixels which are indicating exposed fresh rock due to landsliding. The lateral edges were estimated according to the differences or lineation in vegetation and drainage patterns. The toes of the slopes were bounded by the streambed. Thereafter, the areas of the polygons were rapidly calculated by ArcGIS software (ESRI 2015).

Landslide volume estimation

Digital elevation models were produced by the software MATCH-T DSM (Inpho 2009) using the coregistered

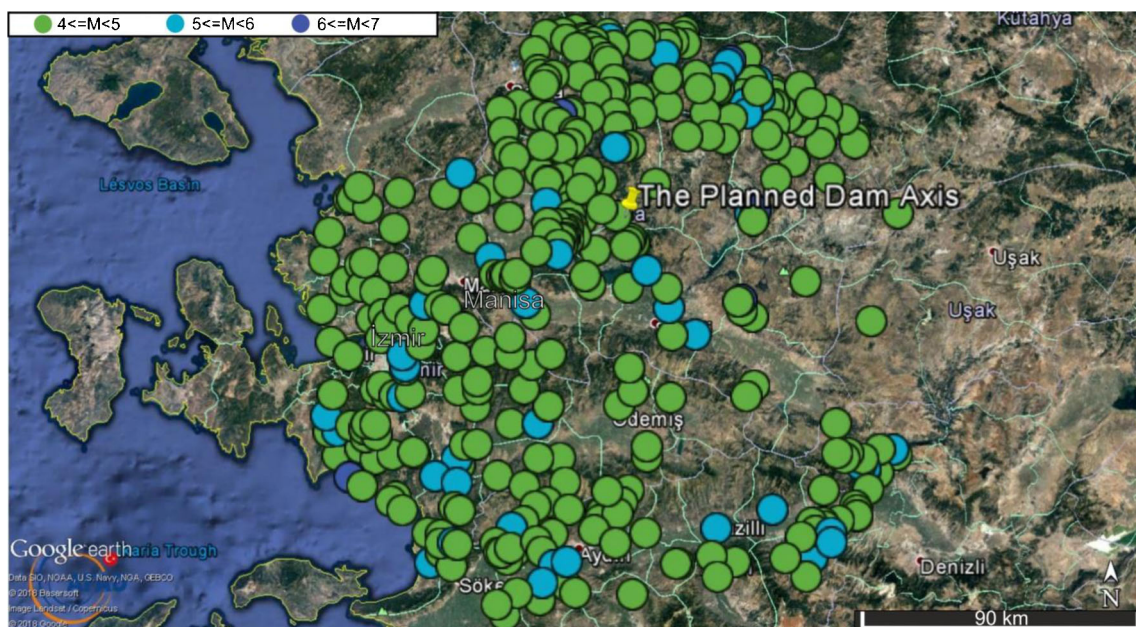


Fig. 10 The distribution of earthquakes occurred in the radius of 100 km of the dam site

Table 1 The selected earthquakes out of 373 to be evaluated in terms of triggering factor

Date/Time	Moment magnitude (M_w)	Distance to epicenter (R) (km)	Depth (km)
24.12.2005/03:56	4.4	16.9	7.5
21.09.1996/03:34	4.2	13.0	4
23.10.1985/06:14	4.4	16.9	12
18.04.1982/23:56	4.7	14.5	10
28.03.1969/01:48	6.5	40.0	4
30.09.1965/19:36	5.0	2.4	10
19.09.1965/14:03	4.4	13.0	10
04.01.1949/20:30	5.1	15.7	14
05.02.1942/01:15	5.7	25.3	10
23.05.1937/10:57	5.7	24.7	10
13.01.1926/08:08	5.9	33.2	10
02.02.1913/06:30	5.2	14.3	10
14.07.1910/02:35	5.0	18.2	10
22.06.1907/16:00	5.1	25.2	10

stereopairs of aerial photographs and automatically collected ground control points. The resultant pixel size of the 1953, 1970, 1995, and 2012 DEMs are 10 m, 20 m, 10 m, and 10 m, respectively. The DEM of 1970 partially includes Landslide-1. Therefore, Landslide-1 was evaluated for the two periods between 1995 to 2012 and 1953 to 1995.

Differential DEM was produced by subtracting the successive DEMs. On the basis of AHDM proposed by Chen et al. (2006), the causes of errors in landslide volume calculations are due to the shifts in plane positions between two images and systematic height differences between two DEMs. Therefore, the differential DEMs were controlled for the systematic height differences between successive DEMs. In this context, sub-areas from different locations (residential areas, farmlands) with various sizes (1284 to 34,785 m²) outside the landslide prone area were selected. The variety in the number and location of the sub-areas were reported to be affecting the average height adjustment value (Chen et al. 2014). Thus, choosing the ideal elevation control sub-areas is a problem. Various numbers of sub-areas (1 to 12) were examined in order to obtain an optimum number of sub-areas (Fig. 11). The histogram of the height difference data provided the average value. The average height differences are considered to be systematic height errors between successive DEMs. As a consequence, different orders of average error were obtained for the years between 1970–1953, 1995–1970, 1995–1953,

and 2012–1995. The differential DEMs were then adjusted for these average height differences by the aid of minus or plus tools in ArcGIS software (ESRI 2015).

The four landslide polygons were extracted from the adjusted differential DEMs. Following this, collapsed and accumulated material volumes within the landslide polygons were calculated by “measure cut and fill” command in Global Mapper software (Blue Marble Graphics 2016). The principle of the calculation is simple and it is time saving. The negative (cut) and positive (fill) elevation difference values of each pixel were multiplied by the pixel area via software automatically. As a result, the collapsed and accumulated material volumes were estimated for each landslide polygon for the periods 1970–1953, 1995–1970, and 2012–1995. The collapsed (cut) material volume was considered to be the volume of material slid into the reservoir. In addition, the effect of image to image coregistration and height adjustment on the calculated depleted and accumulated volumes was revealed.

Cross-sectional analyses

The interpretation of aerial photograph may lead to errors in identifying the limits of landslide body when the size of the landslide is small when compared to the scale of aerial photographs (Mantovani et al. 1996; Metternicht et al. 2005; Singhroy 2002; Guzzetti et al. 2012). In addition, acquisition

Table 2 The acquisition parameters of aerial photographs

Date	Camera	Focal length (mm)	Color	Scale/resolution
1953	Unknown	99.91	Black and white	1/35000
1970	RC5/RC8	151.86	Black and white	1/20000
1995	RC10	153.29	Black and white	1/20000
2012	Multispectral camera (UltracamEagle)	79,800	Digital, colored	0.3 × 0.3 m

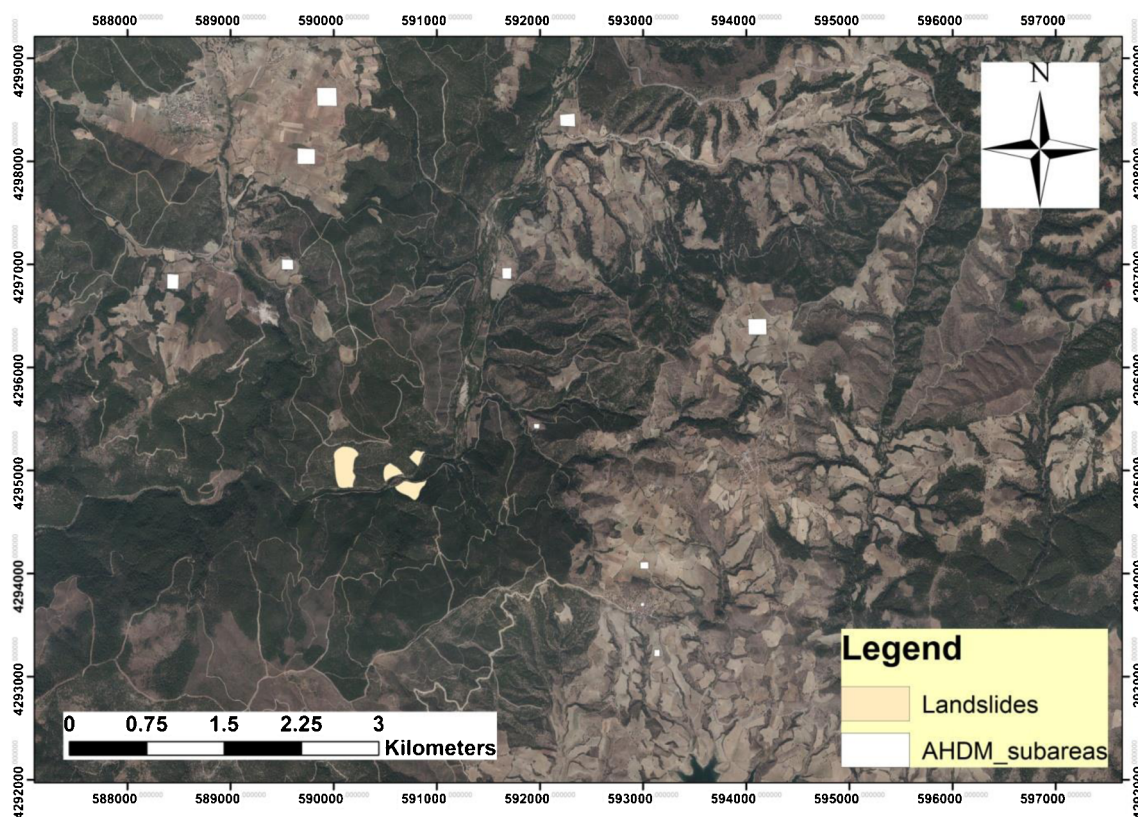


Fig. 11 The sub-areas in the region to determine the average height error between images

date, camera type, scale, and scanner resolution of film-based aerial photographs have an impact on the accuracy of interpretation of landslides. Therefore, the errors in the limits and parts of the landslide body due to the mentioned parameters were controlled by examining depletion and accumulation zones through cross-section profiles extracted from DEMs. In addition, overlapped cross-section profiles serve as an illustrative material for topographical changes. In this context, longitudinal cross-sections passing through the digitized polygons for each year were extracted by Global Mapper software (Blue Marble Graphics 2016) (Fig. 12).

Two successive cross-section profiles overlapped each other for three periods (2012–1995, 1995–1970, 1970–1953) for each landslide. The average error values obtained from the AHDM were also used to adjust the height values in overlapped cross-section profiles. The overlapped cross-section profiles provided information on the limits of landslide body which is indiscernible on aerial photographs. In the case of absence or partial presence of accumulation zone, the initial digitized polygon of the landslide should be extended in the direction of movement in order to involve the accumulation zone detected in overlapped cross-section profiles. In this context, another distinct (secondary) polygon at the toe of the landslide was digitized on the related differential DEM (Fig. 13). The secondary polygon at the toe involves both negative and positive changes in height. There is a strong

possibility that the negative changes in height are due to fluvial erosion. Therefore, only the accumulated volume is calculated within the secondary polygon and added to the initial calculated “fill” volume. Otherwise, the depleted material volume can be overestimated.

In the case of absence or partial presence of depletion zone, the initial digitized polygon of the landslide should be extended in the opposite direction of movement (from the upper hill-slope) in order to involve the depletion zone detected in overlapped cross-section profiles (Fig. 14). A secondary polygon for depletion was digitized on the related differential DEM. In contrast to former application, both depleted and accumulated volumes were considered within the secondary polygon and added to the initial calculated “cut” and “fill” volume.

Results and discussion

Field investigations

The discontinuity planes are smooth undulating, partly iron stained and opened, unfilled and partly filled with clayey material. The Neogene-aged rocks were classified as in the range of medium strong to weak rock. The in situ permeability tests indicated that the Neogene-aged sedimentary rocks are highly permeable (mean permeability coefficient: 9.49×10^{-2} cm/s)

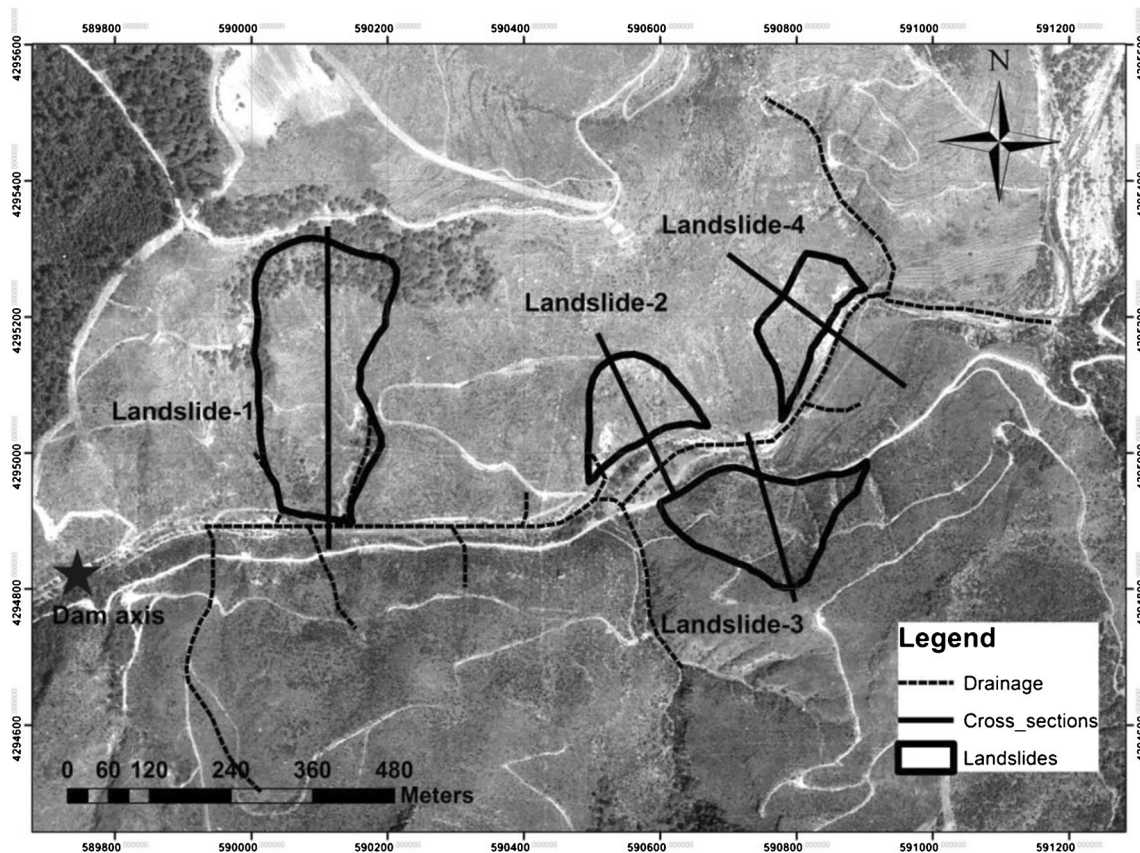


Fig. 12 The cross-section lines taken from the midpoint of the polygons

and partially very slightly permeable due to the locally existing clayey limestone inter-layers (mean permeability coefficient: 2.15×10^{-7} cm/s). The permeability values showed that the permeability rises with low rock quality. The unconsolidated slope debris is also high permeable (mean permeability coefficient: 2.66×10^{-1} cm/s). Therefore, the high

permeability of slope debris causes the underlying weak sedimentary rock layers to be saturated after prolonged rainfalls. However, groundwater level was defined in boreholes at more than 13 m below the ground level in dry season.

Dip direction and dip angle measurements of total 198 discontinuities were projected on Schmidt net (equal area

Fig. 13 Illustration of drawing secondary polygon for accumulation on the plan view of Landslide-4 with respect to the overlapped cross-section profiles of 1970 and 1995

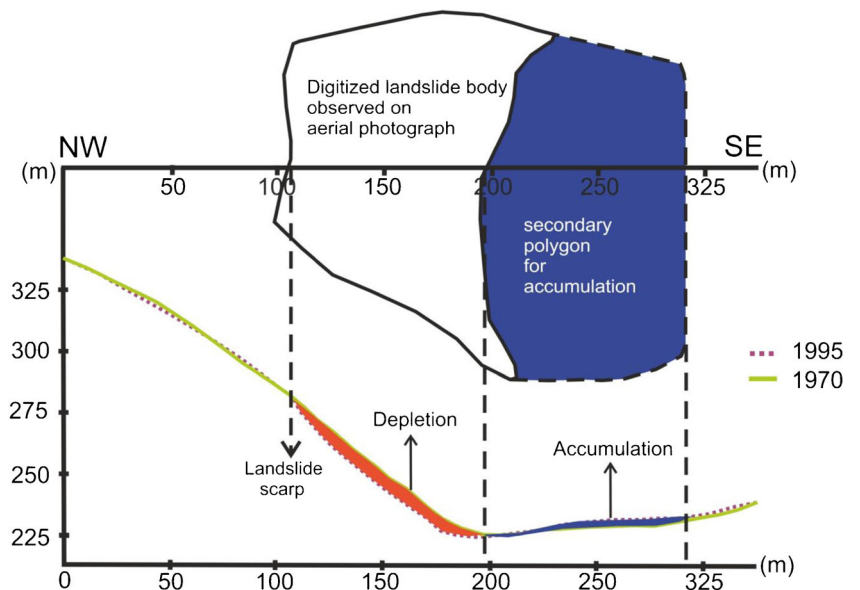
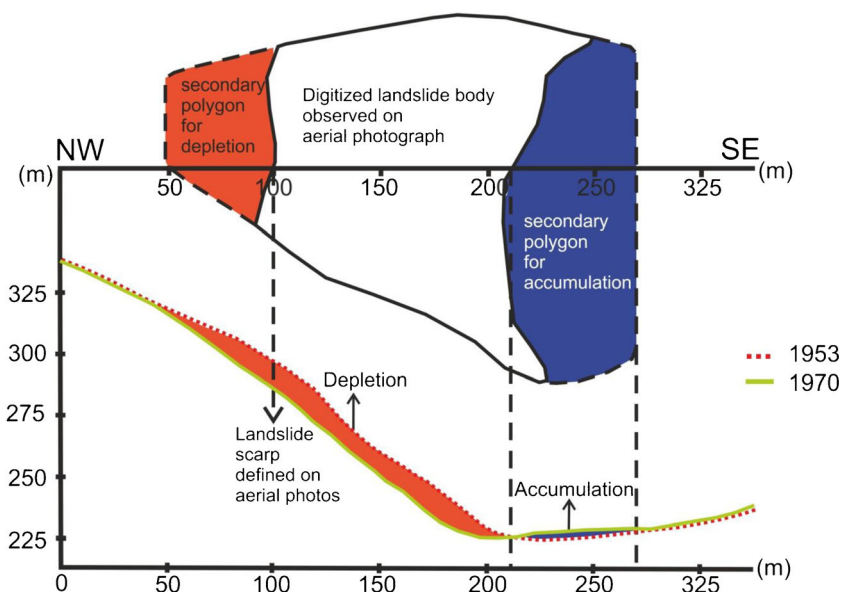


Fig. 14 Illustration of drawing secondary polygon for accumulation on the plan view of Landslide-4 with respect to the overlapped cross-section profiles of 1953 and 1970



projection) (Fig. 15). Pole concentration points of five joint sets and three bedding planes were determined on the Schmidt net. It can be said that the rock mass is highly fractured and prone to rotational failure.

The bedding set-1 and 2 are daylighting on the southern and northern slope faces, respectively. Joint set-4 and 1 are oriented nearly perpendicular to the bedding planes. The vertical joint sets were assumed to work as lateral release surfaces of the sliding mass. The constructed cross-section profile according to borehole and field investigation data indicated that the rock slope failures occur in the highly fractured sedimentary rocks including the slope debris.

Interpretation of aerial photos

The main scarps of Landslide-2 and 4 were clearly identified by the aid of exposed, partly vegetated terrain whereas the main scarps of Landslide-1 and 3 were densely vegetated and could only be identified by the lineation of the vegetation as well as the height differences and convexities. The main scarps were identified even in the oldest aerial photo. Therefore, the first occurrence of the landslides were assumed to be before 1953; however, it is unknown that at which moment the landslides reactivated and which triggering factors featured in reactivations after 1953.

All surface features indicated a rotational type of movement (arcshaped scarp, bulging at the foot, etc.). Landslides with surface areas of 1.55×10^4 to 7.29×10^4 m² were digitized as polygons on each photograph. The area of landslide polygons provided information about the evolution of slope failures quantitatively (Table 3). According to Table 3, minor changes in the area of the landslides between 1953 and 2012 were determined. It can therefore be said that the main landslide body is always active in the lower order of the initial

failure. However, minor scarps were not recognized on aerial photographs except 2012 photograph. 2012 digital photograph partly allowed identifying the minor scarps in the downslope of landslides. Nevertheless, the precise limits of reactivations could not be identified.

Cross-sectional data

Prior to volume calculations, cross-sections were extracted from DEMs of each year. The overlapped cross-section profiles of 1953 and 1970 as well as 1995 and 1970 indicated that the accumulation zone of Landslide-4 is not involved within the digitized polygon (Figs. 13 and 14). Accordingly, no accumulated material volume can be calculated for Landslide-4. Topographical comparison between 1953 and 1970 also revealed that there is a scarp 63 m behind the main scarp which was not observed on the aerial photograph (Fig. 14). The overlapped cross-section profiles of 1995 and 1970 highlighted that the reactivations are the repeated development of the same type of movement which occur in different scarps in the main landslide body. In other words, reactivations are independent movements of portions of the initial displaced mass.

The topographical changes between 1995 and 2012 for Landslide-4 indicated that the heaving in the toe may refer to the possibility of a future landslide event (Fig. 16).

Landslide volumes

Various numbers of sub-areas with varying sizes from different locations were used in determining average height error between two DEMs. Figure 17 shows that 11 sub-areas can produce average height errors independent from their size and location for the DEMs used in this study. The average errors from 11 sub-areas for the periods 1970–1953, 1995–1970,

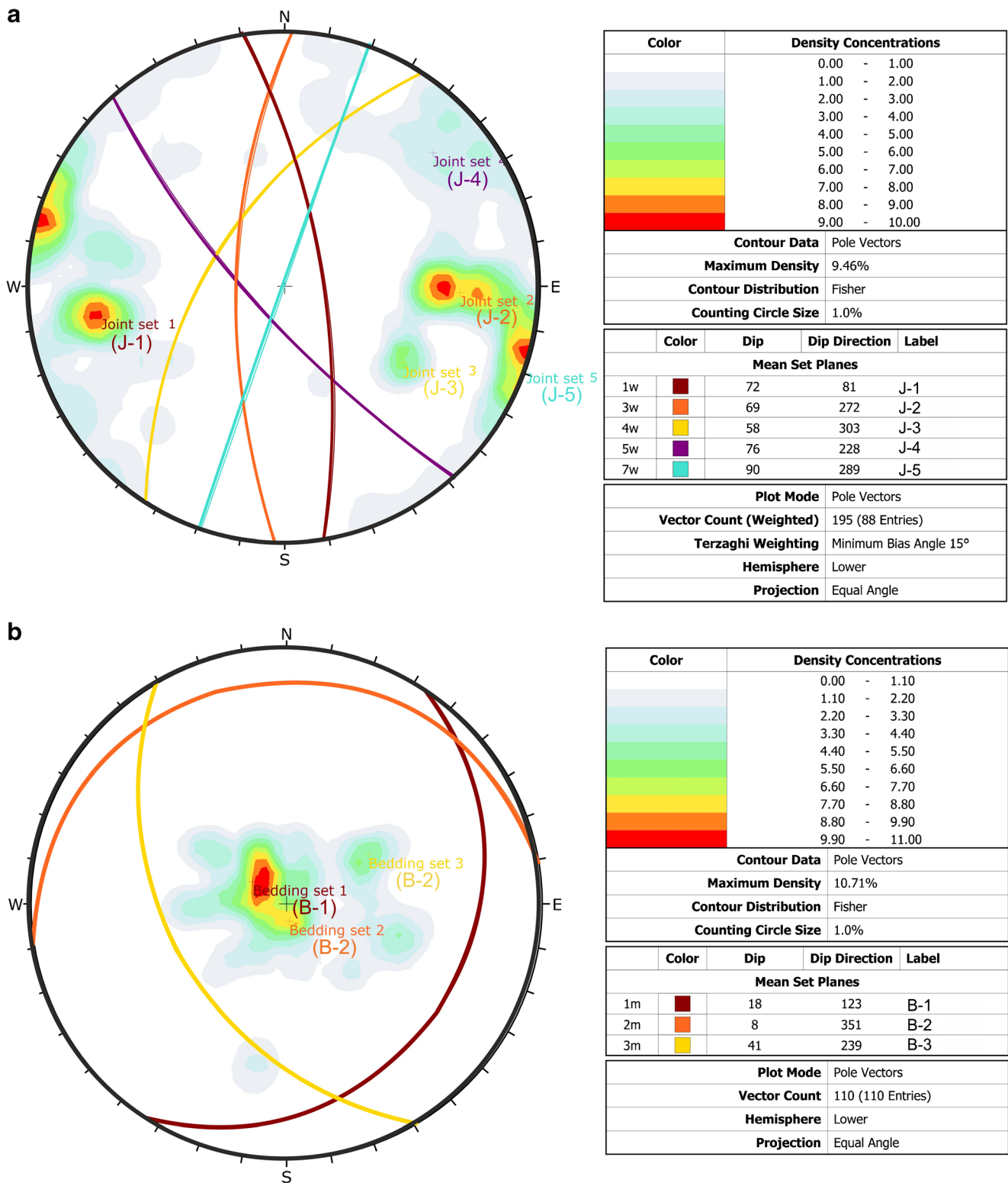


Fig. 15 The contour map of a joint and b bedding planes and great circles of the pole concentration points drawn by Dips software (Rocscience 2010)

1995–1953, and 2012–1995 were obtained as + 25, - 15, - 5, and + 21, respectively. The differential DEMs were then adjusted for these average errors.

The image to image coregistration and height adjustment processes improved the accuracy of the differential DEMs. Table 4 shows that the both methods have a significant effect

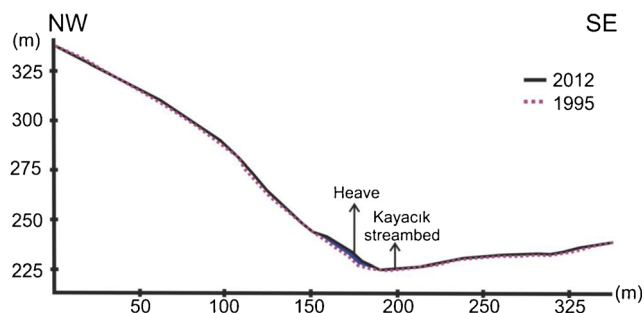
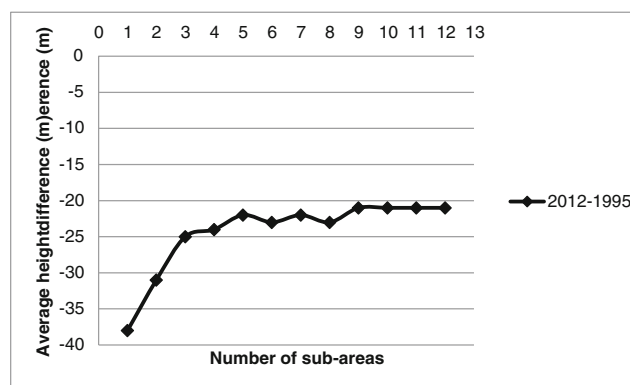
Table 3 The landslide areas calculated with respect to the digitized polygons

	Area (m ²)			
	Landslide-1	Landslide-2	Landslide-3	Landslide-4
2012	72,909	18,785	31,800	16,640
1995	65,226	17,511	31,290	15,544
1970	63,086	16,484	29,889	16,460
1953	72,334	18,842	30,092	16,366

on differential DEMs and thus on volume estimation. Table 4 also indicates that the depth of depletion is in harmony with the breccia zone intersected in the BH-32 and BH-33 (9–23 m).

As a result of AHDM with increased number of sub-areas, differential DEMs of 2012–1995, 1995–1970, and 1970–1953 were produced (Fig. 18). It was confirmed from Fig. 18 that the reactivations occurred in the different portions of the initial landslide body. The accumulation and depletion zones are randomly distributed in the landslide polygons. For example, deposited material at the head of the Landslide-2 between 1970 and 1995 is probably due to the eroded surface material transported from the upper slope face. The depletion zones are present in the lower and middle hillslopes for different periods.

Finally, the collapsed (cut) and accumulated (fill) volumes within the digitized landslide polygons and secondary polygons were estimated (Table 5). A total of 121.78×10^4 m³ material collapsed and 68.50×10^4 m³ material accumulated between the years 1953 and 2012. The total cut and fill volumes preliminary indicated that the mass balance is not reached. In other words, the volume of collapsed material is not equal to the accumulated volume. The total cut volume is commonly greater than the fill volume whereas the order of the difference between cut and fill volumes varies in different periods (Table 5). These results also showed that the long-term annual average (1953–2012) of 2.06×10^4 m³ landslide material has slid into the reservoir area.

**Fig. 16** The cross-sections of Landslide-4 showing the differences in topography between 2012 and 1995**Fig. 17** The change in average height difference between two successive DEMs with respect to the number of sub-areas

Evaluation of triggering and predisposing factors of old landslides

The landslides in the study area can be characterized by continuous movement with fluctuations in landslide mobilization rate due to extensive rainfall, seismic activity, and wildfire. However, it is unknown that at which time the reactivations occurred.

Results indicated that the largest volume of material was removed in the period of 1953 to 1970. As the magnitude and depth of earthquake and the distance between epicenter and affected area are both considered, it can be relevant to the Alaşehir earthquake that occurred in 1969 with a moment magnitude of 6.9 at approximately 40 km south of the dam site. It should be noted that the landslides due to this earthquake can not be evaluated as co-seismic or post-seismic.

The lowest amount of material collapsed in the years between 1995 and 2012 whereas the accumulated material volume is proportionally higher than the other periods. Similar result was obtained in Van Westen and Getahun (2003) and Chen et al. (2006). Van Westen and Getahun (2003) explained the greater accumulation volume than the depletion volume by a reduction of accumulation area. On the other hand, Chen et al. (2006) refers the excess volume to decompaction. It is probable that the volume of accumulated material can be greater than that of the collapsed material due to decompaction and related increase in porosity. The increase in volume for failed rock mass can be up to 30% of the initial volume. Another possible explanation for the highest percentage of accumulation can be the transportation of eroded surface material into the landslide body from upper parts of the slope due to wildfire that occurred in 1988. Delong et al. (2018) have a similar argument that the accumulated volume can be greater than the eroded volume since surface material from farther up in the catchment can be transported through the study area. The amount of eroded material was considered to be increased by the removal of vegetation by the wildfire since the shear strength of the burned surface material

Table 4 Height differences in differential DEMs before and after image to image coregistration and height adjustment

Period	Height difference (m)					
	Before image to image coregistration		After image to image coregistration		After height adjustment	
	Min.	Max.	Min.	Max.	Min.	Max.
2012–1995	– 38	23	– 30	– 13	– 9	8
1995–1970	– 32	13	– 3	23	– 18	8
1970–1953	– 64	30	– 46	– 12	– 21	13

is reduced (Secci et al. 2014) and the root strength of woody vegetation is lost (Riestedberg and Sovonick-Dunford 1983). In addition, an excessive daily precipitation of 163.5 mm in 1986 was thought to be an effective factor for decreasing the resistance of soil to erosion.

Except the period 1995 to 2012, accumulated (fill) volume was defined to be considerably less than collapsed (cut) volume. The collapsed material which was deposited in the streambed was eroded and transported by the stream flow at different rates. In addition, this fluvial erosion can also contribute to the instability of slopes in long-term period due to undercutting phenomenon as similarly stated by Lacroix et al. (2015). The slope of the accumulation area is another controlling factor of the amount of material transported by the stream flow. As the slope increases, the amount of transportation also increases. Accordingly, the lowest amount of accumulation was calculated for the Landslide-3 where the slope of streambed is 11.3° (Table 5).

Slope gradient was also examined as a predisposing factor of landslides. Slope maps highlighted the landslide scarps and partly the release surfaces (Fig. 19). The steep main scarps and lateral edges of landslides are well correlated with the slope angle of 40°–50°. On the other hand, a geologic differentiation can be made between the landslides based on the critical slope angle. The mean critical overall slope angle determined from cross-sections for Landslide-1, 2, and 4 which are formed of unconsolidated conglomerate and sandstone was found to be 33°. Besides, Landslide-3 is mainly composed of highly fractured clayey limestone which allows rapid infiltration of water during intense rainfalls. Therefore, it fails even though the slope angle is lower than 33°.

Conclusions

Various photogrammetric methods and field survey data were used to estimate the collapsed and accumulated volumes of the four landslides in Çağlayan dam reservoir area. It was determined that the landslides involve sandstone, conglomerate, mudstone, claystone, and limestone intercalations which have inherent anisotropy and heterogeneity and are represented by rotational debris and rock slide. The circular slip surface

cuts both the highly fractured rock mass and the debris material lying above the rock mass. The high permeability of slope debris leads the underlying sedimentary rock layers to become fully saturated after heavy rainfalls. The rock layers are therefore weakened and move downslope.

The first occurrence of landslides were determined to be before 1953 and reactivated with different triggering factors with different rates in the investigated time periods. The most effective triggering factor was determined to be the seismic event that occurred in 1969 which induced movement of largest amount of material. Slope angles associated with slope failures are generally between 20° and 40°. However, interaction of the two or more predisposing and triggering factors can be responsible for slope instabilities. Shorter period of differential DEM that is coinciding pre- and post-event is required for more precise estimation of triggering factors. Differential DEMs and overlapped cross-section profiles revealed that the reactivations did not involve the whole landslide body rather occurred within different portions of the initial landslide body. However, revegetation inhibits identifying the secondary scarps related to reactivations on the aerial photographs. Thus, identification of the depletion and accumulation zone of the initial landslide body is prone to errors due to misleading effect of vegetation and poor resolution and shadows in the aerial photograph. It is therefore necessary to construct cross-sections to control the limits of the landslide boundary before employing AHDM to estimate the volume of a landslide more precisely. The overlapped cross-section profiles of Landslide-4 indicated that the polygon boundaries may not involve both accumulation and depletion zones. Despite the fact that cross-section profiles enabled identifying accumulation and depletion zones, major limitation of using this method is being subjective in drawing the lateral limits of secondary polygons.

The volume of landslide material slid into the dam reservoir area which is corresponding to collapsed material volume that was determined based on AHDM proposed by Chen et al. (2006). Despite the original AHDM, average height errors were determined from increased number of sub-areas on successive DEMs. It is suggested that 11 sub-areas can provide accurate height adjustment value independent from the size and location of the sub-areas. The comparison between the

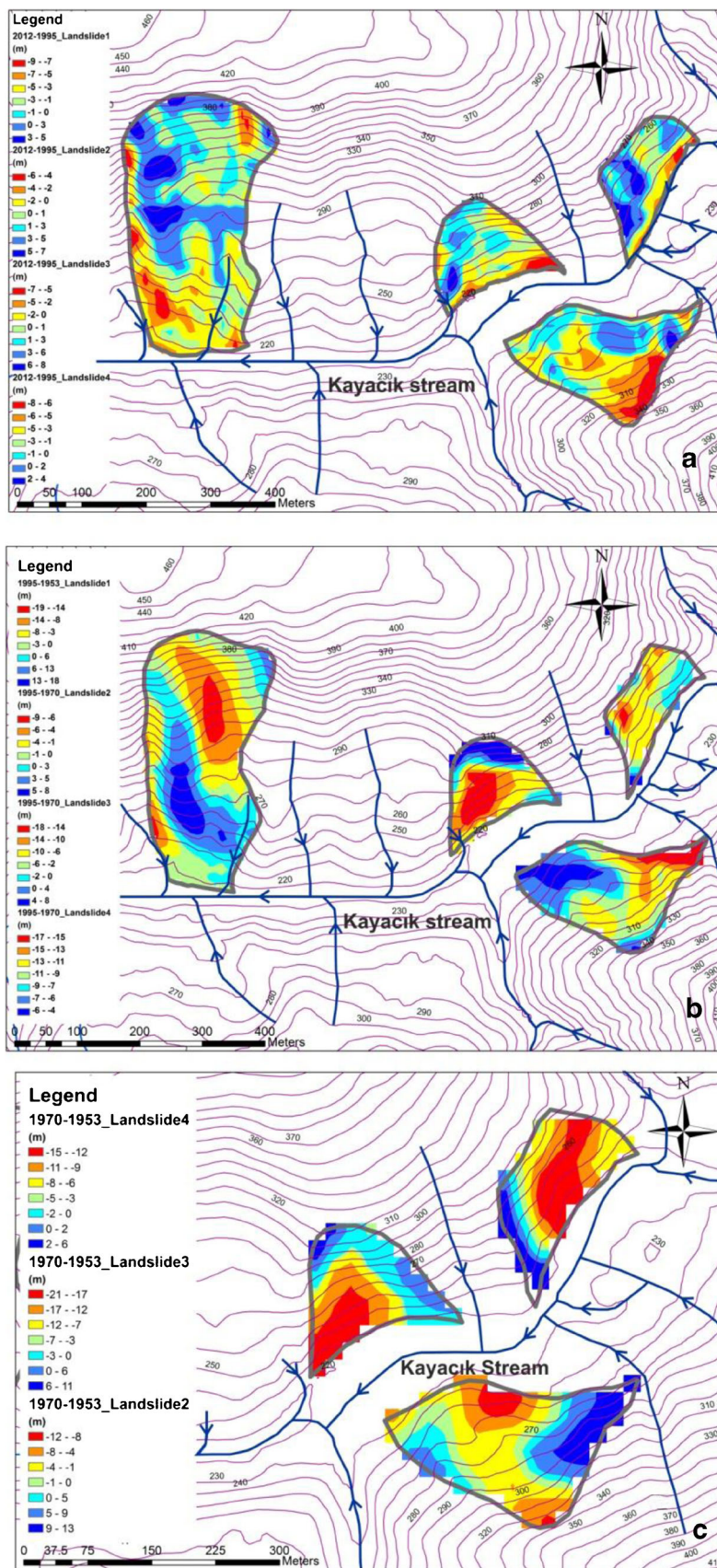


Fig. 18 The differential DEMs of a 2012–1995, b 1995–1970, and c 1970–1953

Table 5 Collapsed (cut) and accumulated (fill) volumes for each landslide for the time periods

Period	Landslide-1		Landslide-2		Landslide-3		Landslide-4	
	Volume ($\times 10^4 \text{ m}^3$)							
	Cut	Fill	Cut	Fill	Cut	Fill	Cut	Fill
2012–1995	15.07	11.35	1.42	2.01	3.96	3.24	2.81	3.45
1995–1970			5.24	2.27	14.63	3.13	12.6	4.92 (0*)
1970–1953			6.25	3.17	20.18	3.94	15.66 (14.2*)	7.52 (0*)
1995–1953	23.96	17.3						
Mean slope of streambed (°)	8.97		5.21		11.3		6.67	

*Before cross-sectional analyses

differential DEMs of before and after image to image coregistration and height adjustment processes has shown that the accuracy of the differential DEMs were improved. It can therefore be assumed that the combination of both methods is a reliable tool for landslide volume estimation.

Taken together, the results of this study reveal that the slopes in the reservoir area are in critical state that may fail by triggering due to fluctuations in the dam reservoir level

after construction, extensive rainfalls, and seismic activities. As the main scarps of landslide bodies are expected to remain below or partly above the estimated maximum water level of dam lake, critical state of slopes will be disturbed. According to the amount of material removed between 1953 and 2012 with an average mobilization rate of $2.06 \times 10^4 \text{ m}^3/\text{year}$, future landslides will not have a destructive effect on the dam structure. However, the collapsed material will contribute to

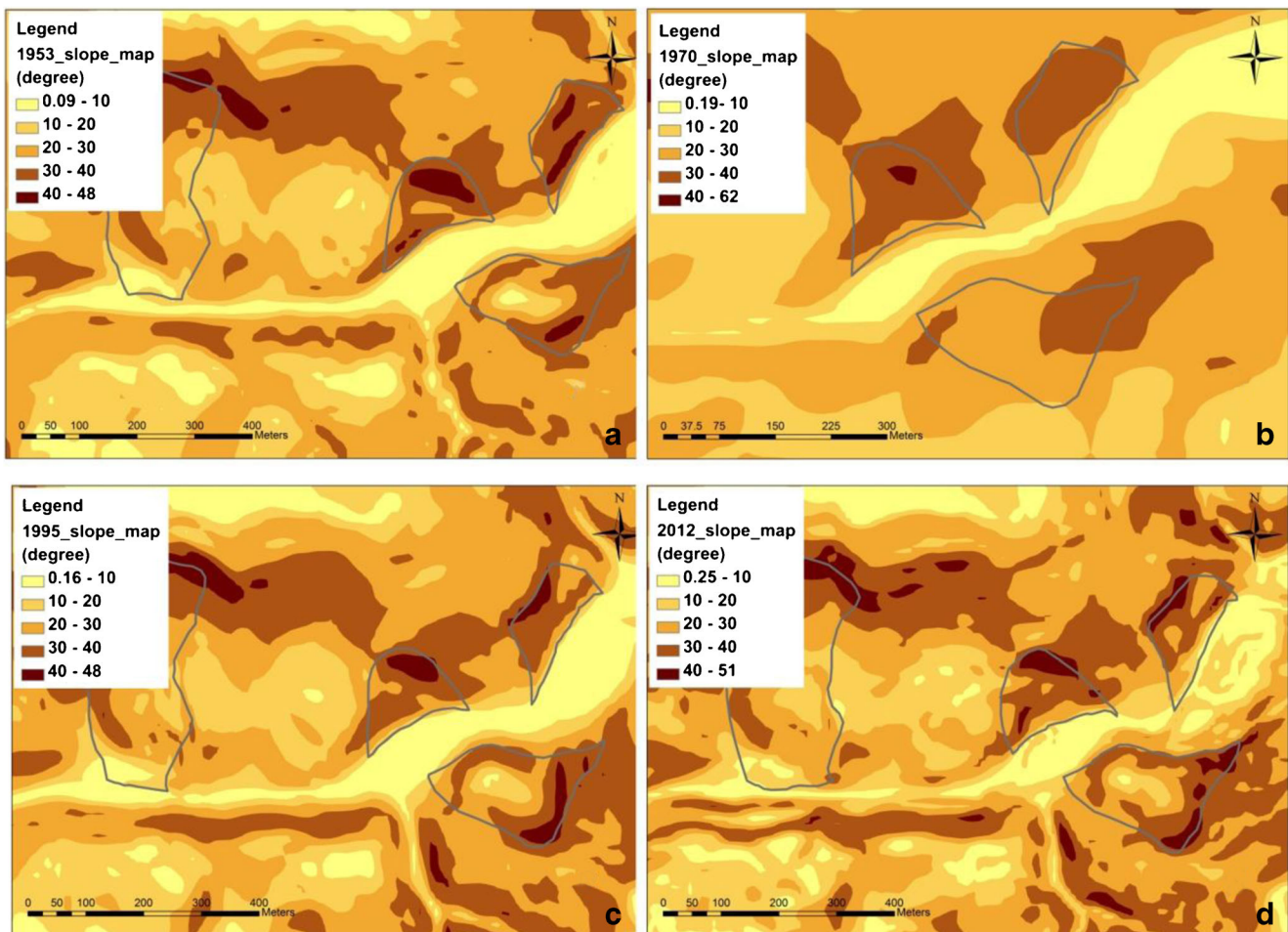


Fig. 19 The slope maps of each year. **a** 2012. **b** 1995. **c**1970. **d** 1953

siltation and thus lead to loss of storage, and shorten the operational life of dam.

Although the methods used in this study gave reasonable landslide volumes, a further research is required to account for error estimation by comparing the results of this study with in situ testing methods to measure the displacement of continuous or single mass movement.

Acknowledgements The borehole data were provided from the General Directorate of State Hydraulic Works in Turkey. The aerial photographs were obtained from General Command of Mapping in Turkey. Precipitation, temperature, and earthquake records were derived from Turkish State Meteorological Service and Disaster & Emergency Management Authority Presidential of Earthquake Department, respectively. We would like to thank to Prof. Dr. Yusuf Kurucu for his assistance and contributions during the project and to the EMİ Group Information Technologies Corporation for collaboration in DEM generation from historical aerial photographs.

Funding information This research was funded by Dokuz Eylül University under the project number 2012.KB.FEN.044.

References

- Amirahdi A, Pourhashami S, Karami M, Akbari E (2016) Modeling of landslide volume estimation. *Open Geosci* 8:360–370
- Ayoub F, Leprince S, Avouac J (2009) Co-registration and correlation of aerial photographs for ground deformation measurements. *ISPRS J Photogramm Remote Sens* 64:551–560
- Bai S, Wang J, Thiebes B, Cheng C, Yang Y (2013) Analysis of the relationship of landslide occurrence with rainfall: a case study of Wudu County, China. *Arab J Geosci* 7(4):1277–1285
- Blue Marble Geographics (2016) Global Mapper software version 18
- Cai F, Ugai K (2004) Numerical analysis of rainfall effects on slope stability. *Int J Geomech* 4(2):69–78
- Chen RF, Chang KJ, Angelier J, Chan YC, Deffontaines B, Lee CT, Lin ML (2006) Topographical changes revealed by high-resolution airborne LiDAR data: the 1999 Tsaoiling landslide induced by the Chi-Chi earthquake. *Eng Geol* 88:160–172
- Chen Z, Zhang B, Han Y, Zuo Z, Zhang X (2014) Modeling accumulated volume of landslides using remote sensing and DTM data. *Remote Sens* 6:1514–1537
- Coe J, Glancy P, Whitney J (1997) Volumetric analysis and hydrologic characterization of a modern debris flow near Yucca Mountain, Nevada. *Geomorphology* 20:11–28
- Corsini A, Borgatti L, Cervi F, Dahne A, Ronchetti F, Sterzai P (2009) Estimating mass-wasting processes in active earth slides-earth flows with time-series of high-resolution DTMs from photogrammetry and airborne LiDAR. *Nat Hazards Earth Syst Sci* 9:433–439
- Cruden DM, Varnes DJ (1996) Landslide types and processes. In: Turner AK, Schuster RL (eds) *Landslides: investigation and mitigation*. Transportation Research Board, Special Report No 247, 36–75
- De Bari C, Lapenna V, Perrone A, Puglisi C, Sdao F (2011) Digital photogrammetric analysis and electrical resistivity tomography for investigating the Picerno landslide (Basilicata region, southern Italy). *Geomorphology* 133:34–46
- DeLong SB, Youberg AM, DeLong WM, Murphy BP (2018) Post-wildfire landscape change and erosional processes from repeat terrestrial lidar in a steep headwater catchment, Chiricahua Mountains, Arizona, USA. *Geomorphology* 300:13–30
- Du JC, Teng HC (2007) 3D laser scanning and GPS technology for landslides earthwork volume estimation. *Autom Constr* 16:657–663
- Duman TY, Çan T, Emre Ö (2011) 1/1.500.000 Turkey Landslide Inventory Map, General Directorate of Mineral Research and Exploration special publications series-27, Ankara, Turkey
- Emre Ö, Duman TY, Özalp S, Elmacı H, Olgun Ş, Şaroğlu F (2013) 1/1.250.000 Turkey Live Fault Map, General Directorate of Mineral Research and Exploration special publications series, Ankara, Turkey
- Environmental Systems Research Institute (ESRI) (2015) ArcGIS software version 10.4.1
- Fuller JC, Riedler AR, Bell R, Marden M, Glade T (2016) Landslide-driven erosion and slope channel coupling in steep, forested terrain, Ruahine Ranges, New Zealand, 1946–2011. *Catena* 142:252–268
- Gabet EJ (2003) Post-fire thin debris flows: sediment transport and numerical modelling. *Earth Surf Process Landf* 28:1341–1348
- Ghafoori M, Lashkaripour GR, Tarigh Azali S (2011) Investigation of the geological and geotechnical characteristics of Daroongar Dam, Northeast Iran. *Geotech Geol Eng* 29:961–975
- Guzzetti F, Ardizzone F, Cardinali M, Galli M, Rossi M, Valigi D (2009) Landslide volumes and landslide mobilization rates in Umbria, Central Italy. *Earth Planet Sci Lett* 279:222–229
- Guzzetti F, Mondini AC, Cardinali M, Fiorucci F, Santangelo M, Chang KT (2012) Landslide inventory maps: new tools for an old problem. *Earth Sci Rev* 112:42–66
- Hack R, Alkema D, Kruse GAM, Leenders N, Luzi L (2007) Influence of earthquakes on the stability of slopes. *Eng Geol* 91(1):4–15
- Hakyemez HY, Göktaş F, Erkal T (2013) Quaternary geology and evolution of the Gediz graben. *Geol Bull Turkey* 56(2):1–26 (in Turkish)
- Huang Y, Yu M, Xu Q, Sawada K, Moriguchi S, Yashima A, Liu C, Xue L (2015) InSAR-derived digital elevation models for terrain change analysis of earthquake-triggered flow-like landslides based on ALOS/PALSAR imagery. *Environ Earth Sci* 73(11):7661–7668
- IAEG Commission on Landslides (1990) Suggested nomenclature for landslides. *Bull Int Assoc Eng Geol* 41(1):13–16
- Inpho (2009) Inpho GmbH Match-T DSM software version 5.2
- ISRM (2007) The complete ISRM suggested methods for rock characterization, testing and monitoring: 1974–2006. In: Ulusay R, Hudson JA (eds) *Suggested methods prepared by the Commission on Testing Methods, ISRM*, Compilation arranged by the ISRM Turkish National Group, Kozan Ofset, Ankara
- Lacroix P, Berthier E, Maquerhua ET (2015) Earthquake-driven acceleration of slow-moving landslides in the Colca valley, Peru, detected from Pléiades images. *Remote Sens Environ* 165:148–158
- Larsen IJ, Montgomery DR, Korup O (2010) Landslide erosion controlled by hillslope material. *Nat Geosci* 3:247–251
- Lu L, Wang ZJ, Song ML, Arai K (2015) Stability analysis of slopes with ground water during earthquakes. *Eng Geol* 193:288–296
- Malamud BD, Turcotte DL, Guzzetti F, Reichenbach P (2004) Landslides, earthquakes, and erosion. *Earth Planet Sci Lett* 229:45–59
- Mantovani F, Soeters R, Van Westen CJ (1996) Remote sensing techniques for landslide studies and hazard zonation in Europe. *Geomorphology* 15:213–225
- Marchesini I, Cencetti C, De Rosa P (2009) A preliminary method for the evaluation of the landslides volume at a regional scale. *Geoinformatica* 13(3):277–289
- Martinović K, Gavin K, Reale C, Mangan C (2018) Rainfall thresholds as a landslide indicator for engineered slopes on the Irish Rail network. *Geomorphology* 306:40–50
- Metternicht G, Humi L, Gogu R (2005) Remote sensing of landslides: an analysis of the potential contribution to geo-spatial systems for hazard assessment in mountainous environments. *Remote Sens Environ* 98:284–303

- Nikolaeva E, Walter TR, Shirzaei M, Zschau J (2014) Landslide observation and volume estimation in Central Georgia based on L-band InSAR. *Nat Hazards Earth Syst Sci* 14:675–688
- Özkaymak Ç, Sözbilir H, Uzel B (2013) Neogene-Quaternary evolution of the Manisa Basin: evidence for variation in the stress pattern of the İzmir-Balıkesir Transfer Zone, western Anatolia. *J Geodyn* 65: 117–135
- PCI Geomatics (2012) PCI Geomatica software version 12.0.1
- Riestenberg MM, Sovonick-Dunford S (1983) The role of woody vegetation in stabilizing slopes in the Cincinnati area, Ohio. *Geol Soc Am Bull* 94(4):506–518
- Rocscience Inc. (2010) Dips v.6.0. Graphical and statistical analysis of orientation data
- Secci R, Calcina SV, Ranieri G, Uras G (2014) Analysis of the stability variation of a slope crossed by forest fire. *Int J Civ Eng* 3(1):41–50
- Singhroy V (2002) Landslide hazards: CEOS, the use of earth observing satellites for hazard support: assessments and scenarios. Final report of the CEOS Disaster Management Support Group, NOAA, pp 98
- Thornthwaite CW (1948) An approach toward a rational classification of climate. *Geogr Rev* 38(1):55–94
- Tsutsui K, Rokugawa S, Nakagawa H, Miyazaki S, Cheng C, Shiraishi T, Yang S (2007) Detection and volume estimation of large-scale landslides based on elevation-change analysis using DEMs extracted from high-resolution satellite stereo imagery. *IEEE Trans Geosci Remote Sens* 45(6):1681–1696
- Ulusay R, Tuncay E, Sönmez H, Gökçeoğlu C (2004) An attenuation relationship based on Turkish strong motion data and iso-acceleration map of Turkey. *Eng Geol* 74:265–291
- Van Westen C, Getahun F (2003) Analyzing the evolution of the Tessina landslide using aerial photographs and digital elevation models. *Geomorphology* 54:77–89
- Vardon PJ (2015) Climatic influence on geotechnical infrastructure: a review. *Environ Geotech* 2(3):166–174
- Wang B, Vardon PJ, Hicks MA (2018) Rainfall-induced slope collapse with coupled material point method. *Eng Geol* 239:1–12
- Yu M, Huang Y, Xu Q, Guo P, Dai Z (2016) Application of virtual earth in 3D terrain modeling to visual analysis of large-scale geological disasters in mountainous areas. *Environ Earth Sci* 75(7):1–7